Tailoring fiber dispersion and mechanical properties in strain-hardening alkali-activated composite through viscosity adjustment and casting methodologies

Ge, Zhi; Song, Haomeng; Wang, Jinlong; Wang, Zhong; Zhang, Hanming; Zhang, Hongzhi; Šavija, Branko

Contents lists available at ScienceDirect

Construction and Building Materials

journal homepage: www.elsevier.com/locate/conbuildmat

Tailoring fiber dispersion and mechanical properties in strain-hardening alkali-activated composite through viscosity adjustment and casting methodologies[☆]

Zhi Ge [a], Haomeng Song [a], Jinlong Wang [b], Zhong Wang [b], Hanming Zhang [a], Hongzhi Zhang [a,*] [ID], Branko Šavija [c] [ID]

[a] *School of Qilu Transportation, Shandong University, Jinan 250002, China*
[b] *Water Resources Research Institute of Shandong Province, Jinan 250002, China*
[c] *Faculty of Civil Engineering and Geosciences, Delft University of Technology, Delft, CN 2628, the Netherlands*

A B S T R A C T

This paper aims at enhancing tensile properties of strain-hardening alkali-activated composite (SHAAC) by using a flow-induced casting approach. $Ca(OH)_2$-activated ground granulated blast-furnace slag (GGBS) was used as binder material and viscosity modifying admixture (VMA) was applied to adjust the rheology. Combined X-ray computed tomography (X-CT) scanning and image analysis were proposed to obtain the spatial distribution of polyvinyl alcohol (PVA) fibers in hardened SHAAC prepared with various VMA dosages using different (i.e. conventional and flow-induced) casting approaches. The results revealed optimal rheological properties (yield stress of 192 Pa, plastic viscosity of 17.6 Pa·s) of paste for fiber distribution and alignment. The SHAAC with fiber distribution and orientation factors of 0.91 and 0.83 was prepared using the flow-induced casting approach with a WMA dosage of 1.0 %. Its ultimate tensile stress and tensile strain capacity reached 6.1 MPa and 5.5 %, respectively, which was 37 % and 36 %, more than the conventionally cast SHAAC. In the end, an empirical equation for ultimate tensile strength and strain capacity prediction with high determination coefficient was proposed based on fiber distribution, orientation, and porosity.

1. Introduction

Strain-hardening cementitious composite (SHCC) represents a kind of short fiber-reinforced cementitious composite that is characterized by its unique capacity to exhibit multiple cracking and strain-hardening gain with exceptional deformation capacity under tension [1,2]. Application of SHCC to the key part under tension has the capacity to significantly raise the toughness and durability of concrete infrastructure.

In the absence of coarse aggregate, SHCC requires a high-volume of Portland cement (PC). Due to serious environment issues, sustainable binder material is required to take place of Portland cement. Alkali-activated composites have been considered as a promising candidate [3]. Industrial byproducts including ground-granulated blast furnace slag (GGBS) and fly ash (FA) constitute the primary raw materials for alkali-activated composites [4]. Sodium hydroxide and Sodium

metasilicate solutions maintain widespread preference as alkaline activator due to the effective activation performance [5,6]. Nedeljković et al. [7] developed Strain-hardening alkali-activated composite (SHAAC) by using sodium silicate solution-activated GGBS/FA reinforced with fibers and applied it in a canoe. Wang et al. [8] developed SHAAC containing various fiber volume fractions and evaluated the influence of PVA fiber dosage on the mechanical behavior of SHAAC. However, it has been noted that the combination of NaOH and Na_2SiO_3 solutions releases substantial thermal energy, and thus controlled cooling periods are necessary prior to mixing. Besides, the management of corrosive activator solutions remains a persistent obstacle in transitioning from laboratory to industrial-scale production. Powdered activators (e.g., $Ca(OH)_2$, anhydrous Na_2SiO_3) are therefore employed in lieu of traditional liquid activators [9]. Shi et al.[10] demonstrated that $Ca(OH)_2$-activated GGBS materials can be employed as concrete binders due to their cost-effectiveness and good durability. Choi et al. [11]

developed SHAAC by using Ca(OH)$_2$-activated GGBS reinforced with PVA fibers, demonstrating clearly strain-hardening behavior accompanied by crack saturation phenomena.

The remarkable multiple cracking and strain hardening behavior of SHAAC is mainly attributed to the fiber-bridging ability [12]. Generally, approximately 2 %vol fiber is used [13]. The dispersed fibers function as microscale reinforcement, preventing the progression of microcracks and retarding the initiation of macrocracks, while also providing an interfacial transition zone (ITZ) which serves as a source of cracking sites [14,15]. The fibers normally used in SHAAC can be bent or coiled during casting, resulting in fiber clustering and non-uniform dispersion, further affecting fiber dispersion and alignment characteristics within the matrix. [16]. The crack-bridging performance of fibers within SHAAC matrix exhibits strong dependence on both distribution and alignment of the fibers in relation to the applied loading directions [17, 18]. Therefore, significant research efforts are devoted to improving the fiber distribution and alignment to enhance the mechanical performance of SHAAC.

The rheological properties of the binder are the most critical factor affecting the fiber distribution and orientation [19,20]. Yield stress and plastic viscosity have been often used to characterize the rheological properties of SHAAC matrix [21]. Li et al. [22] demonstrated the correlation between the rheological parameters, PVA fibers distribution, and tensile properties, identifying a specific flow rate range that enhances both fiber distribution and tensile strain capacity. According to Tosun-Felekoğlu et al. [23], a more cohesive matrix lead to more uniform fiber distribution and better fiber alignment along the SHAAC flow direction. Conventionally, the rheological properties of SHAAC have been achieved through mix proportion modifications, including binder selection, optimization of key parameters (specifically water-to-binder (W/B) and sand-to-binder (S/B) ratios), and controlled addition of chemical admixtures [24–26]. Considering that the binder composition, W/B and S/B in SHAAC are typically designed based on micro-mechanics, adjusting admixture dosage emerges as the most feasible approach owing to its minimal impact on matrix mechanical properties. Tang et al. [27] explored the combined effects of viscosity modifying admixtures (VMA) and superplasticizer (SP) on the rheology of SHAAC. Proper rheology and optimal SP-VMA dosages were identified for enhancing mechanical performance, yet quantitative analysis of fiber dispersion within the matrix has not been conducted. In addition to modifying matrix rheological properties, a flow-induced approach has been proposed to improve fiber distribution and alignment [28,29]. This approach has demonstrated practical value for thin-slab structure under unidirectional tension or bending, such as steel bridge deck and road pavements [30]. Similarly, the extrusion-based technique has been used in 3D-printed SHAAC [31,32]. When the fibers are forced through this narrow nozzle, their alignment follows the movement direction of the nozzle [33]. The alignment of fibers relies on a variety of factors like the wall effect of the nozzle [34], nozzle size [35], specimen shape [36], matrix rheology [37], and the properties of fiber [38].

However, fiber distribution and orientation and their correlation with rheological properties and flow-induced approach were not quantitatively characterized. The characterization of fiber spatial distribution has been the subject of extensive research, with several methods having been employed. By directly observing the fibers on the fracture plane of SHAAC, the fiber orientation factor can be calculated, yet this approach usually requires a great deal of work [39,40]. An alternative approach is Scanning Electron Microscopy (SEM). SEM is capable of generating detailed images of the fiber distribution on the specimen's surface [41]. The 2D characterization is insufficient in capturing the comprehensive spatial information of the fibers within the specimen and leading to inaccurate assessments of the fiber distribution and alignment. With the evolution of non-destructive testing techniques, several research employs the 3D visualization method of X-ray Computed Tomography (X-CT) to characterize fiber distribution [42,43]. Oesch et al. [44] examined the distribution of steel fibers within matrix based on X-CT.

However, PVA fibers can distort and deform within the matrix [45]. Moreover, the grayscale values of the fibers in the X-CT images are rather similar to those of other components. This similarity significantly complicates the segmentation and identification of fibers, thereby compromising the accuracy and reliability of the characterization.

In this paper, a flow-induced casting approach was adopted to improve the fiber distribution and tensile performance of a sustainable SHAAC prepared with Ca(OH)$_2$-activated GGBS reinforced with PVA fiber. An image processing procedure was proposed to quantitatively characterize the distribution of PVA fibers combined with X-CT scanning. The effects of rheological properties and casting approach on fiber distribution and mechanical properties were investigated. An empirical equation considering fiber distribution, orientation, and porosity for tensile properties prediction was developed.

2. Experimental

2.1. Materials and mix proportions

The ingredients include ground-granulated blast-furnace slag (GGBS), calcium carbide slag (CCS), quartz sand, superplasticizer, viscosity modifying admixtures (VMA), defoaming agent, water and Polyvinyl alcohol (PVA) fiber. The particle size distribution of GGBS (S95) is presented in Fig. 1(a). CCS is an alkaline waste material, comprising more than 80 % calcium hydroxide (Ca(OH)$_2$). The elemental compositions of GGBS and CCS determined through X-ray fluorescence (XRF) tests are summarized in Table 1. Fine aggregate consisted of quartz sand (particle size range 60–100 μm, median particle size 80 μm).

The bulk density of the quartz sand was determined to be 1.54 g/cm^3, and the particle size characteristics are detailed in Fig. 1(b). Admixtures involved 150,000-viscosity hydroxypropyl methylcellulose (HPMC) VMA and polycarboxylic acid-based superplasticizer (SP) demonstrating 20 % water reducing capacity. The PVA fiber used were purchased from Kuraray. Table 2 lists its mechanical and physical properties.

CCS was used as activator for GGBS. VMA was used to modify the rheology of the matrix. The VMA had a pH of 9.5 ± 1.0 and a density of 0.930 ± 0.030 kg/m^3. Table 3 lists the mix proportions of SHAAC, maintaining constant mass ratios of GGBS/CCS (7.2), water/binder (0.4), and sand/binder (0.3) for all proportions. With a consistent 2.0 vol% fiber content, specimens with four different VMA dosages, i.e., 0.5 %, 1.0 %, 1.5 %, 2.0 %, and two casting approaches, i.e., conventional casting (R-), and flow-induced casting (O-) were prepared, as shown in Table 3.

2.2. Mixing and casting process

The SHAAC specimens were prepared using a standardized mixing process. The binding components including GGBS and CCS were combined with quartz, VMA and defoaming agent were firstly mixed together in a planetary mixer with low-speed (140 rpm) for 3 minutes. The SP and water were added, followed by a medium-speed (285 rpm) for 5 minutes. PVA fibers were then introduced, with continued mixing for another 5 minutes.

Two distinct casting approaches (i.e., conventional and flow-induced) were used. The conventional approach involved direct placement of fresh mixture into molds, producing reference specimens termed as R-SHAAC. Regarding the flow-induced approach, a flow-induced casting device was utilized to improve the fibers alignment along the flow path, with the resulting specimens labeled as O-SHAAC.

The flow-induced casting device was a bespoke extrusion device, as illustrated in Fig. 2(a). It integrated three functional components: material feeding, extrusion control, and flow-induction. The feeding assembly featured a conical hopper integrated with a screw pump (extrusion) for controlled material pouring. A tube with a diameter of 100 mm (flow-induction), was linked to the screw pump to establish
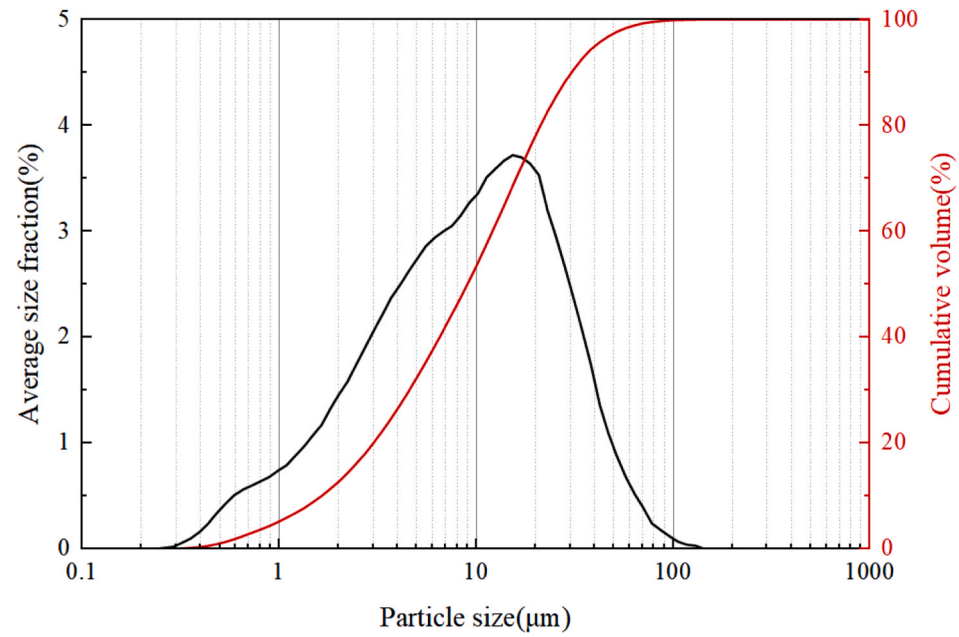
(a)
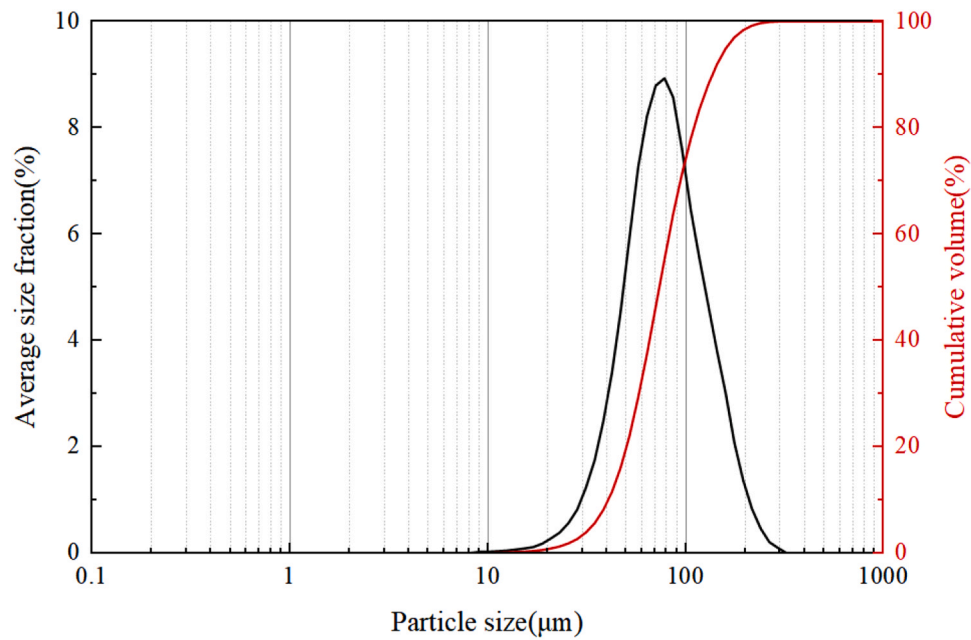
(b)

Fig. 1. The particle size distribution of (a) GGBS and (b) quartz sand.

Table 1
Chemical components of GGBS and CCS (%).

Chemical compositions	CaO	SiO$_2$	Al$_2$O$_3$	MgO	SO$_3$	TiO$_2$	MnO	Fe$_2$O$_3$	etc
GGBS	41.28	32.65	13.87	6.92	2.76	0.78	0.47	0.44	0.83
CCS	88.86	6.00	2.58	0.06	1.62	0.05	0.01	0.59	0.23

directional casting path. To optimize fiber alignment along the flow direction, the terminal section of tube was equipped with a steel nozzle (100 mm wide and 10 mm high) [41].

Fig. 2(b) illustrates the dumbbell mold used for uniaxial tensile test and casting direction. Specimen has a tensile region with a length of 80 mm and a cross-sectional area of 30 mm by 13 mm within this

Table 2

The mechanical and physical properties of PVA fiber.

Fiber type	Length (mm)	Diameter (μm)	Elastic modulus (GPa)	Tensile strain (%)	Tensile strength (MPa)	Density (g/cm^3)
PVA fiber	12	40	41	6.5	1600	1.3

region. Two layers were cast using the steel nozzle at an extrusion rate of 0.09 m/s for the dumbbell specimen. Surface-smoothing and moisture retention using plastic film were carried out after casting. Demolding was performed after 24 hours. Curing was conducted under controlled environmental conditions (23 ± 3°C temperature, 98 ± 2 % RH) for 28 days prior to mechanical testing.

2.3. Test programs

2.3.1. Rheological tests

It is expected that fiber alignment is influenced by the rheology of fresh mixes. The flow curves of fresh paste (without fibers) with VMA dosages of 0.5 %,1.0 %, 1.5 % and 2.0 % was measured using Brookfield RST-CC rheometer. The rheological testing was conducted as follows: firstly, the rheometer rotor was installed and adjusted to ensure full immersion in the paste. Then, paste was prepared without fibers and poured into the rheometer container. The shear procedure as illustrated in Fig. 3 was then conducted to achieve the flow curves as the function of shear stress varying with shear rate. For every mix, the test was carried out 3 times, and the mean value was used.

2.3.2. Uniaxial tensile test

For the uniaxial tensile test, three dumbbell specimens per condition were subjected to loading at a speed of 0.2 mm/min. Digital Image Correlation (DIC) was employed to control the loading rate and analyze the strain in the gauging zone (80 × 30 mm^2). The DIC equipment (Fig. 4 (a)), positioned 300 mm away from the specimen surface on one side, incorporates two cameras (binocular system) that simultaneously capture images of the tested specimen's surface from different angles. Two pairs of reference markers were attached to the specimen at the ends of the central part, where the distance between the measurement points was 80 mm, see Fig. 4(b). The position change of each reference marker

was traced and average deformation rate of the two pair gauges was used for the loading rate control. The gauging zone (80 × 30 mm^2) was sprayed with a speckle pattern (Fig. 4(b)) to facilitate full-field strain visualization and crack behavior analysis during loading. The continuous photo capturing interval was set as 0.2 s. For DIC processing, the subset size was set to 50 pixels, and the step size was set to 5 pixels.

2.3.3. X-CT and image process

Combined X-ray computed tomography (X-CT) and image segmentation methodology was employed to acquire the spatial distribution of
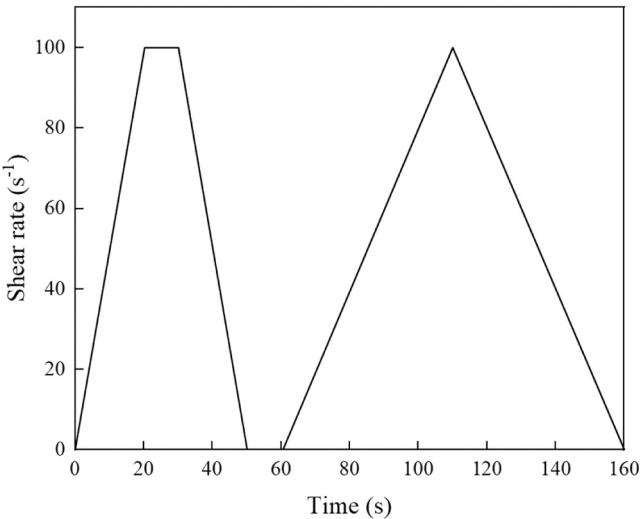
Fig. 3. Shear procedure.

Table 3

Mix proportions of SHAAC (weight ratio).

Mix IDs	CCS	GGBS	Quartz sand	Water	VMA	Superplasticizer	Defoaming Agent	PVA Fiber
R-VMA0.5	0.125	0.875	0.300	0.400	0.005	0.020	0.010	2 % (Vol.)
R-VMA1.0					0.010			
R-VMA1.5					0.015			
R-VMA2.0					0.020			
O-VMA0.5					0.005			
O-VMA1.0					0.010			
O-VMA1.5					0.015			
O-VMA2.0					0.020			

Fig. 2. Schematic description of (a) flow-induced casting device and (b) casting dumbbell specimens. (Unit: mm).

Fig. 4. (a) DIC set up and (b) dumbbell specimen with reference markers and speckle pattern for uniaxial tensile test.

Fig. 5. Cylindrical sample cut from dumbbell specimen (Unit: mm).

fibers in hardened SHAAC. SHAAC prepared with different VMA dosages and casting approaches were characterized. Fig. 5 illustrates that the cylindrical sample, having a diameter of 5 mm and a heigh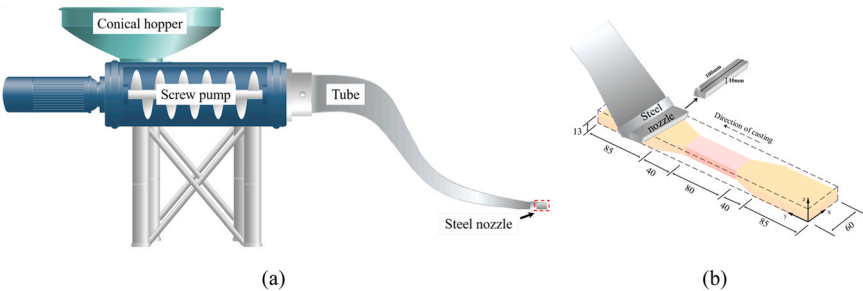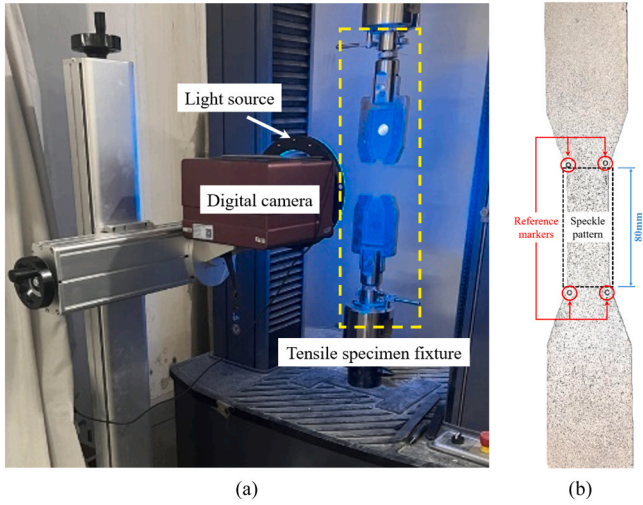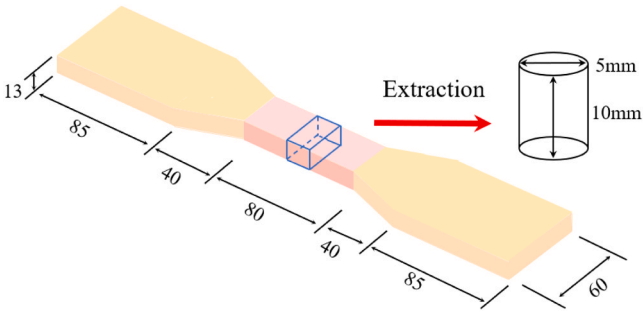t of 10 mm, was drilled from specimen's center. The scanning was carried out using a ZEISS Xradia 510 Versa 3D X-ray microscope. The voltage for scanning was set to 80 kV, with a current of 0.087 mA. The reconstructed voxel resolution was 13.68 μm (almost one third of the PVA fiber diameter), resulting in 731 slices along the Z-axis spanning the 10 mm sample height, with an inter-slice spacing of 13.68 μm.

Grayscale images were imported into AVIZO software for the segmentation process (Fig. 6). A median filter [46,47] was first utilized to reduce noise and smooth the images, as well as to enhance discrimination of substances. Grayscale value was then employed to segment the fibers and matrix following [48,49]. Since the PVA fiber and air void have similar gray values in the CT images, the fibers extracted after segmentation contain a significant number of air voids. A sphericity threshold segmentation [50,51] approach was employed to eliminate isolated air voids. In this approach, the sphericity of the independent models was calculated using Eq. 1 [52]:

$$S_p = \frac{\sqrt[3]{36\pi V^2}}{A} \tag{1}$$

where S_p is the sphericity; V represents the volume of individual particles, while A denotes the particle surface area. If S_p is 1, it signifies that the particle is a standard sphere.

Models with a sphericity less than 0.7 was defined as fibers and models with a sphericity greater than 0.7 were defined as air voids. Afterwards, air voids contacted with fibers were removed by using a template matching method as illustrated in Ref. [53,54]. The derived

spatial distribution of fibers was further used for the orientation characterization.

2.3.4. Characterization of fiber distribution and orientation

A hemispherical model was utilized to characterize the distribution and orientation of fibers. The fiber orientation angle θ characterizes the angular deviation between individual fibers and their horizontal plane projections, corresponding to the flow direction, as illustrated in Fig. 7. The θ can be calculated using the following equations:

$$\theta = \arccos\left(\frac{\sqrt{x_i^2 + y_i^2}}{\sqrt{x_i^2 + y_i^2 + z_i^2}}\right) \tag{2}$$

$$(x_i, y_i, z_i) = (x_l, y_l, z_l) - (x_j, y_j, z_j) \tag{3}$$

where (x_i, y_i, z_i) is the fiber directional vector, (x_j, y_j, z_j) the fiber initial coordinate, and (x_l, y_l, z_l) is the fiber terminal coordinate.

To quantitatively assess the distribution of θ, the orientation factor η was adopted from the methodology developed by Xia et al. [56], with its mathematical formulation presented in Eq. 4.

$$\eta = \int_{\theta_{\min}}^{\theta_{\max}} p(\theta)\cos^2(\theta)d\theta \tag{4}$$

where $p(\theta)$ represents the probability density of fibers being at an angle θ [23]; $\theta_{\max}$ and $\theta_{\min}$ denoting the maximum and minimum fiber orientation angle, respectively. When $\eta = 1$, all fibers align with the casting direction, and when $\eta = 0$, the fibers are all positioned at 90 degrees relative to the casting direction.

The continuous extrusion and mixing movements during the SHAAC preparation process may influence the spatial distribution of fibers. The fiber distribution factor α is used to evaluate the differences in fiber distribution within the matrix, as illustrated in Eq. 5 [57].

$$\alpha = \frac{1}{3}\left(e^{\left[-\frac{1}{x_0}\sqrt{\frac{\sum(x_k - x_0)^2}{n}}\right]} + e^{\left[-\frac{1}{y_0}\sqrt{\frac{\sum(y_k - y_0)^2}{n}}\right]} + e^{\left[-\frac{1}{z_0}\sqrt{\frac{\sum(z_k - z_0)^2}{n}}\right]}\right) \tag{5}$$

$$(x_k, y_k, z_k) = 0.5 \times (x_l, y_l, z_l) + 0.5 \times (x_j, y_j, z_j) \tag{6}$$

where (x_0, y_0, z_0) is the matrix central coordinate; (x_k, y_k, z_k) is the fiber central coordinate; n represents the total count of fibers.

3. Results

3.1. Rheology

Fig. 8 illustrates the flow curves of SHAAC paste with various VMA dosages. Assuming that the fresh SHAAC paste is a non-Newtonian fluid, its rheological behavior can be modeled using the modified Bingham model (Eq. 7)[58].

$$\tau = \tau_0 + \mu\gamma + c\gamma^2 \tag{7}$$

where τ_0 is the yield stress (YS), which is the intercept of the fitted quadratic curve; τ is the shear stress; γ is the shear rate; and μ is the plastic viscosity (PV), which is the coefficient of the linear term. The least-squares method was used to fit the curves.

Table 4 shows the fitting results. The high R^2 confirms that the modified Bingham model is effective to describe the shear stress-rate dependency. Both YS and PV exhibit positive correlation with VMA dosage. Specifically, increasing VMA dosage from 0.5 % to 2.0 % elevates yield stress from 170 to 223 Pa, while YS increases from 15.3 to 22 Pa·s. These indicate that VMA can effectively modify the rheology properties of SHAAC paste.
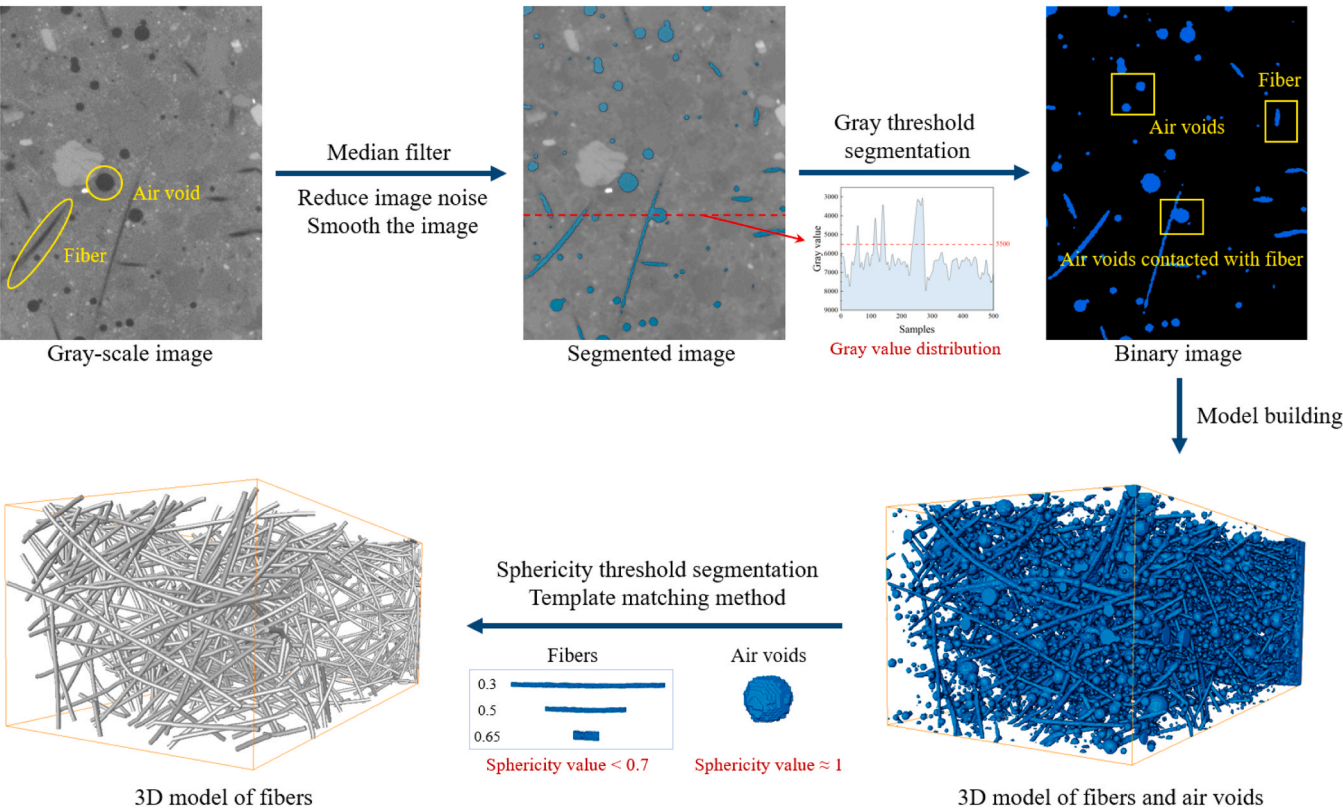
Fig. 6. X-CT image segmentation process.
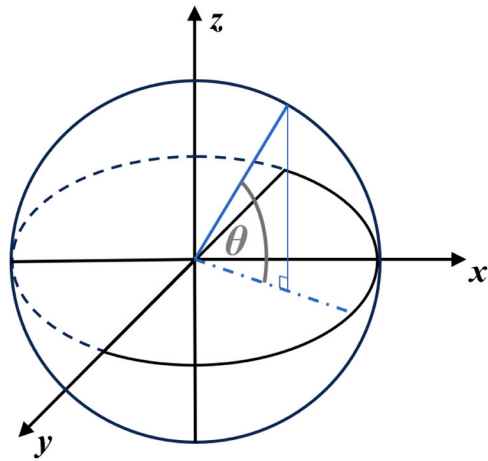
Fig. 7. The fiber orientation factor derivation model [55].

Fig. 8. Flow curve of SHAAC paste with different VMA dosages.

This can be attributed to two primary factors: 1) Bridging effect. As a chain polymer compound, hydroxypropyl methylcellulose possesses reactive moieties capable of adhering to GGBS particulates. These macromolecular chains establish interparticle connections through bridging phenomena, ultimately generating a stabilized three-dimensional framework [59]. 2) Interfacial modification effects. The amphiphilic constituents within hydroxypropyl methylcellulose molecules alter the surface charge distribution of particles, thereby enhancing interparticle attraction forces and leading to particle agglomeration [60].

Table 4
Fitting results of SHAAC paste with 4 VMA dosages ranging from 0.5 % to 2.0 %.

VAM dosage	Fitting equation	R^2	YS (Pa)	PV (Pa·s)
0.5 %	$y = 170 + 15.3x - 0.03x^2$	0.988	170	15.3
1.0 %	$y = 192 + 17.6x - 0.22x^2$	0.995	192	17.6
1.5 %	$y = 207 + 19.3x - 0.13x^2$	0.991	207	19.3
2.0 %	$y = 223 + 22x - 0.05x^2$	0.994	223	22.0

(a) R-VMA0.5 (b) R-VMA1.0 (c) R-VMA1.5 (d) R-VMA2.0
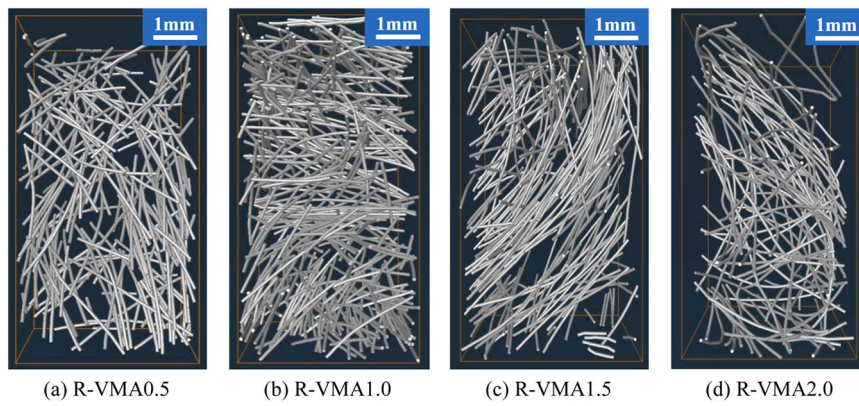
Fig. 9. Spatial distributions of fibers in hardened SHAAC with different VMA dosages obtained using conventional casting approach.

(a) O-VMA0.5 (b) O-VMA1.0 (c) O-VMA1.5 (d) O-VMA2.0

Fig. 10. 3D spatial distributions of fibers in hardened SHAAC with different VMA dosages obtained using flow-induced casting approach.

3.2. Fiber distribution and orientation

The spatial distributions of fibers in hardened SHAAC with various VMA dosages and different casting approaches are illustrated in Fig. 9 and Fig. 10. The distribution and orientation of fibers vary significantly with VMA dosages. As can be seen, a VMA dosage of 1.0 % leads to the most uniform spatial distribution of fibers for both conventional and flow-induced cast specimens.
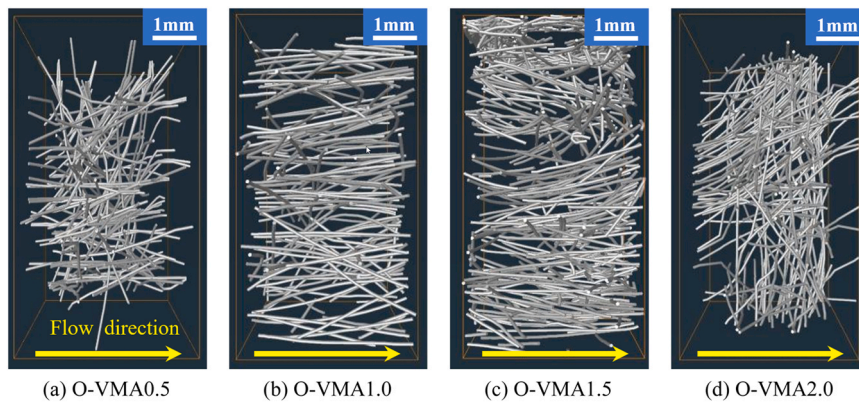
Table 5 lists the total fiber count within each analyzed SHAAC cylindrical sample. The fiber distribution factors are calculated using Eq. 5 and summarized in Fig. 11. The influence of VMA dosage on fiber distribution factor using different approach follows the same trend. In the conventional specimens, compared to the specimens with a VMA dosage of 0.5 %, a VMA dosage of 1.0 % led to an 11 % increase in the fiber distribution factor. However, further increasing the VMA dosage leads to a decrease. This is attributed to the alterations in rheological properties which affects the fiber movement within the matrix. For flow-induced approach, a VMA dosage of 1.0 % generates a fiber distribution factor of 0.91 which is 12 % higher than that of R-VMA1.0, which means the flow-induced process is favorable for the uniform dispersion of fiber.

Fig. 12 plots the probability density distribution function ($p(\theta)$) obtained from fitting the fiber orientation angle distribution. In the
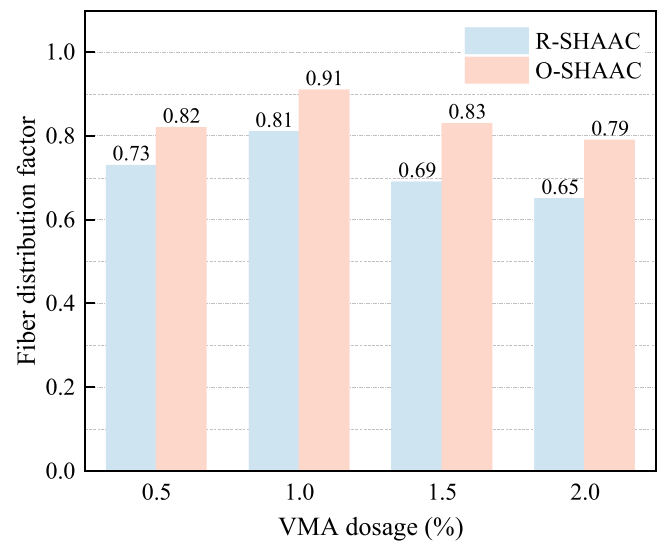
Fig. 11. Fiber distribution factor of SHAAC with different VMA dosages and casting approaches.

conventionally cast specimens, fibers are evenly distributed in the range between 0 and 90°. Conversely, in the flow-induced cast specimens, the majority of fibers demonstrates a fiber orientation angle less than 40°. This suggests that the fibers in the flow-induced specimens exhibit a greater degree of horizontal alignment (0°) compared to the conventional specimens. The orientation of the fibers is quantified using Eq. 4 (Table 6).

Table 5
The total count of fibers.

Mix IDs	The total count of fibers	Mix IDs	The total count of fibers
R-VMA0.5	79	O-VMA0.5	128
R-VMA1.0	102	O-VMA1.0	152
R-VMA1.5	132	O-VMA1.5	152
R-VMA2.0	107	O-VMA2.0	144

(a) Conventional casting

(b) Flow-induced casting

Fig. 12. The probability density distribution function of the fibers in SHAAC with different VMA dosages.

Table 6
Fiber orientation parameters.

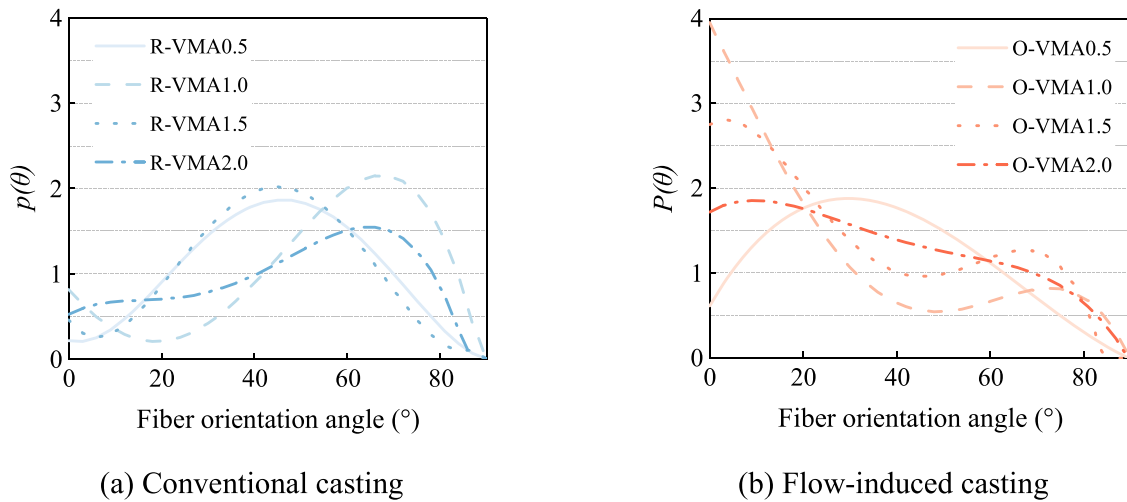| Mix IDs	Fiber average orientation angle	Fiber orientation angle main range	Fiber orientation factor
R-VMA0.5	49°	40°−50°	$\eta= 0.53$
R-VMA1.0	64°	50°−60°	$\eta= 0.57$
R-VMA1.5	55°	50°−60°	$\eta= 0.62$
R-VMA2.0	59°	60°−70°	$\eta= 0.59$
O-VMA0.5	33°	30°−40°	$\eta= 0.62$
O-VMA1.0	5°	0°−10°	$\eta= 0.83$
O-VMA1.5	16°	0°−10°	$\eta= 0.79$
O-VMA2.0	28°	10°−20°	$\eta= 0.71$

Table 6 lists the average fiber orientation angle, the main range of fiber orientation angles and fiber orientation factor. The average fiber orientation angle of flow-induced specimens is observed to be reduced in comparison to conventional specimens. The main range of fiber orientation angle follows the same trend.

When the VMA dosage increases from 0.5 % to 2.0 %, the fiber orientation factors of the conventional specimens are 0.53, 0.57, 0.62, and 0.59, respectively. In instances where flow-induced casting is employed, the fiber orientation factors are increased by 17.0 %, 45.6 %, 27.4 %, and 20.3 %. This is due to the fact that during the extrusion of the SHAAC through the steel nozzle, the nozzle's shape and the wall effect drive the fiber alignment along the flow direction [38]. An explanation of the wall effect is shown in Fig. 13, where the flow velocity changes from zero at the walls to a peak value along the nozzle centerline, causing the fibers to align [37].

The largest improvement on fiber orientation factors occurs at a VMA dosage of 1.0 %. The good dispersion of the fibers enhances the alignment action of the steel nozzle, thus achieving a greater magnitude of influence on fiber orientation, and achieving the best fiber orientation result.
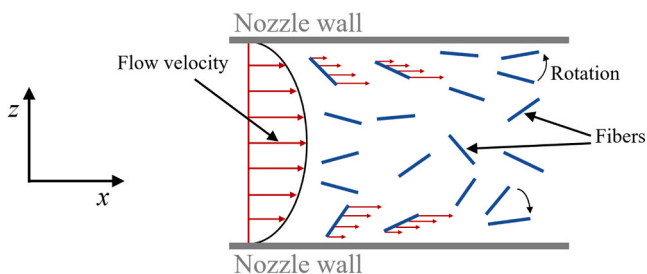

Fig. 13. Schematic explanation of the wall effect in the steel nozzle.

3.3. Relation between matrix rheology and fiber distribution characteristics

Fig. 14 and Fig. 15 clearly reveal the relationships between the rheology index and fiber distribution and orientation. As the VMA dosage increases, the distribution factor of specimens cast by both approaches, along with the fiber orientation factor of flow-induced specimens, initially rises and subsequently declines.

The cause of the aforementioned phenomena is that as the YS and PV increase, the movement of the paste and the interaction of the solid particles in the matrix generate higher shear force. The shear force acts as a guiding force, facilitating the free rotation and dispersion of the fibers [61]. In the flow-induced casting process, when the paste is extruded through the steel nozzle, the fibers align themselves more significantly in the flow direction. However, when the YS climbs to 192 Pa and the PV reaches 17.6 Pa·s, the shear force reaches a critical point at which the shear force manifests as fiber migration resistance, preventing the free rotation of fibers. This is detrimental to the wall effect of the steel nozzle, ultimately leading to a reduction in both the fiber distribution factor and the fiber orientation factor.

In comparison with conventional specimens, the fiber distribution factor increases when the flow-induced approach is employed. This is owing to two main reasons. Firstly, in the flow-induced process, a force generated by the screw pump drives the fibers to disperse within the matrix. Secondly, the steel nozzle imposes certain restrictions on the outward movement of the fibers, which also contributes to a better dispersed state of the fibers within the specimen area, enhancing the fiber distribution factor of specimens.

3.4. Porosity

Fig. 16 shows the porosity of SHAAC derived from X-CT images. In conventional specimens, porosity ranges from 2.0 % to 4.32 %. In flow-
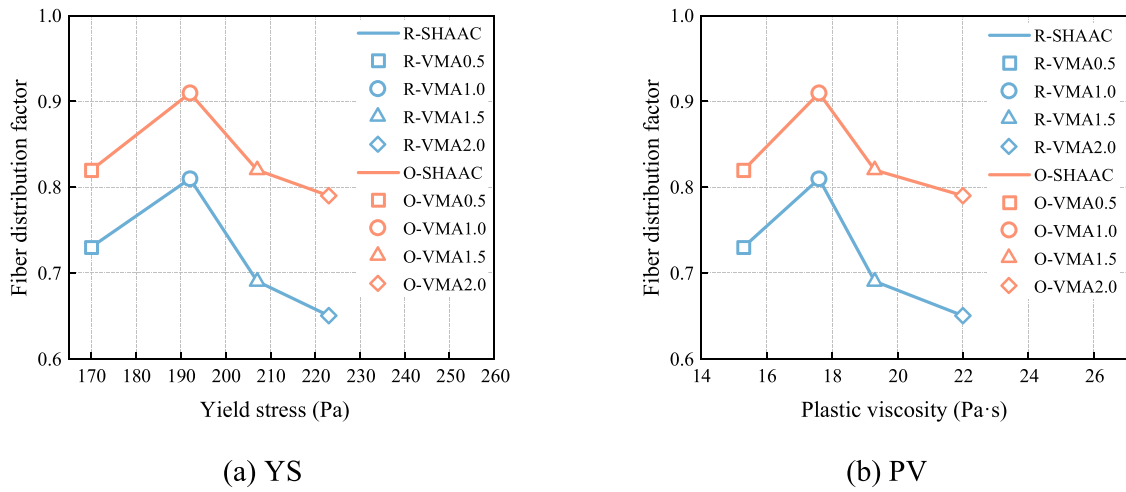
(a) YS

(b) PV

Fig. 14. Fiber distribution factor-Rheology index relationship.
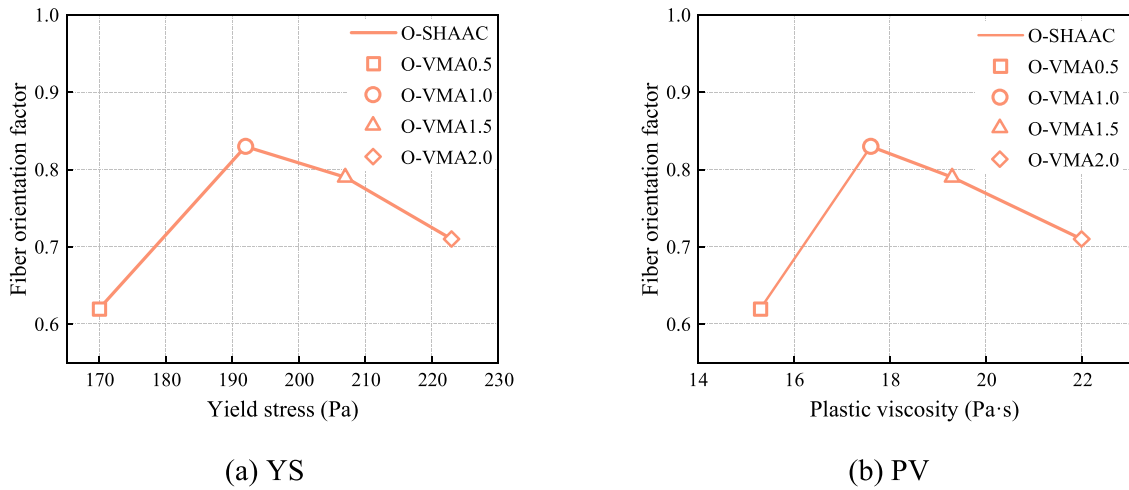

(a) YS

(b) PV

Fig. 15. The relationship between fiber orientation factor of the flow-induced specimens and rheology index.
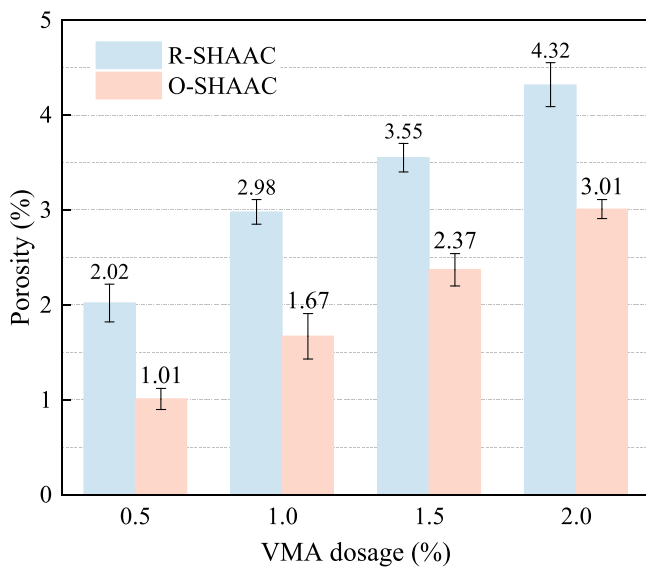

Fig. 16. Porosity of SHAAC with different VMA dosages and casting approach.

induced specimens, the porosity ranges from 1.01 %, to 3.01 %. It is evident that as the VMA dosage increases, the porosity exhibits a progressive increase. The increase in porosity with higher VMA dosages is primarily due to the reduced flowability and increased plastic viscosity, which hinders the efficient escape of air bubbles during mixing and casting [62,63]. The flow-induced specimens demonstrate a lower porosity, indicating that the screw pump and steel nozzle can effectively extrude air of SHAAC paste in the extrusion process. It should be noted that the spatial resolution of 13.68 μm inherently limited the detectability of pore phase below this threshold, leading to a underestimation of total porosity.

3.5. Uniaxial tensile properties

Stress-strain curves of the hardened SHAAC are plotted in Fig. 17. The stress-strain response shows that the all specimens exhibit tensile strain-hardening behavior. Features including cracking strength, ultimate tensile strength, tensile strain capacity, count of cracks, crack width are presented in Table 7.

In the initial phase of the stress-strain curve, the tensile stress increases linearly until the first crack appears, at which point the stress is defined as the cracking strength. The specimen with 1.0 % VMA dosage exhibits superior cracking strength compared to other specimens in both casting approaches. The flow-induced casting approach further increases the cracking strength compared with the conventional approach.
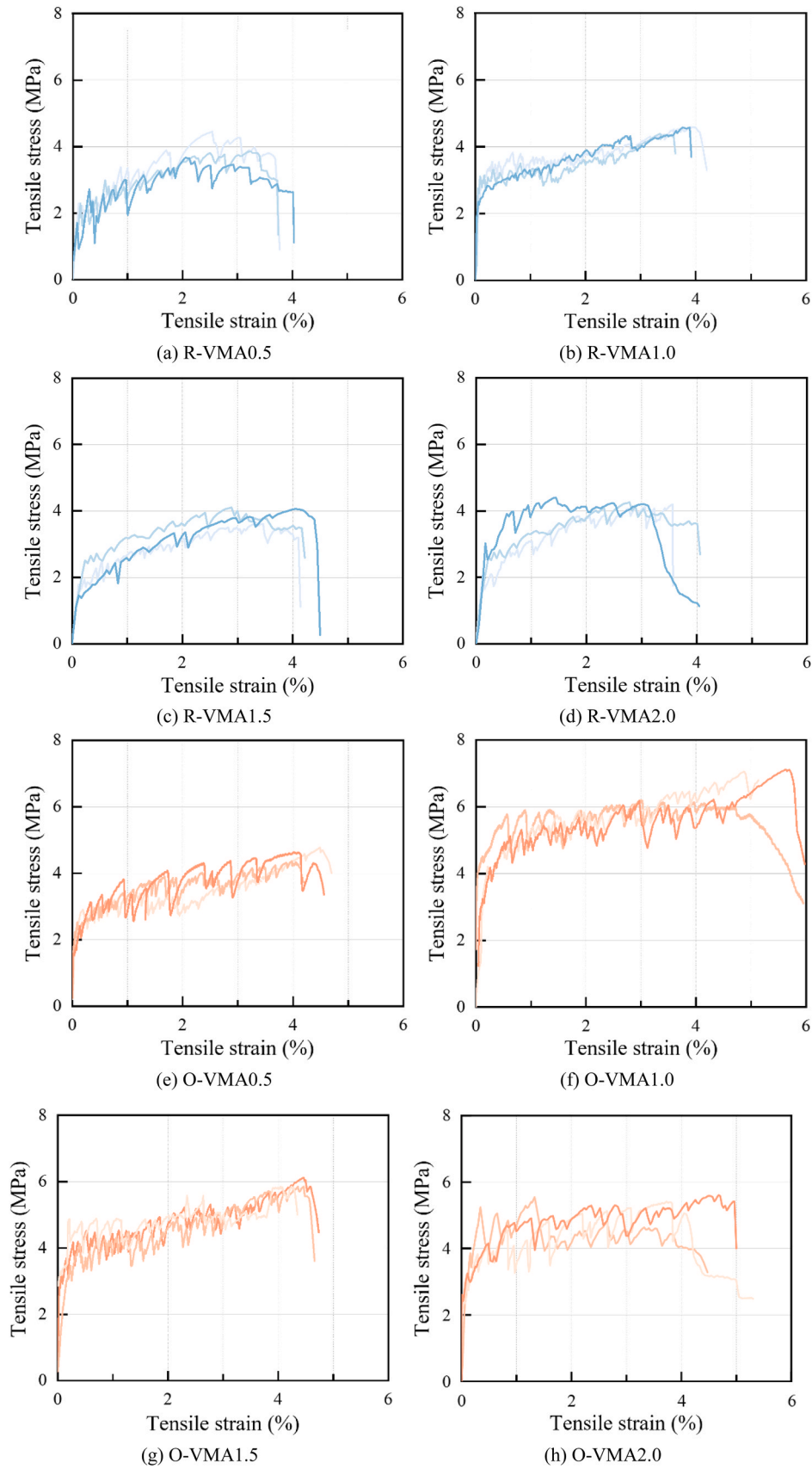
Fig. 17. Tensile stress-strain curves of SHAAC.

Table 7
Summary of tensile properties of SHAAC.

Mix IDs	Cracking strength (MPa)	Ultimate tensile strength (MPa)	Tensile strain capacity (%)	Count of cracks	Crack Width (mm)
R-VMA0.5	2.5 ± 0.1	3.6 ± 0.2	3.8 ± 0.4	18 ± 2	0.178
R-VMA1.0	2.7 ± 0.5	4.5 ± 0.4	4.0 ± 0.5	25 ± 3	0.128
R-VMA1.5	1.8 ± 0.2	3.8 ± 0.2	4.2 ± 0.3	27 ± 2	0.133
R-VMA2.0	2.2 ± 0.1	3.9 ± 0.3	3.7 ± 0.3	22 ± 1	0.136
O-VMA0.5	2.2 ± 0.2	4.0 ± 0.2	4.5 ± 0.3	29 ± 3	0.124
O-VMA1.0	3.8 ± 0.7	6.1 ± 0.9	5.5 ± 0.7	46 ± 2	0.095
O-VMA1.5	2.7 ± 0.4	5.0 ± 0.4	4.8 ± 0.4	37 ± 4	0.108
O-VMA2.0	2.8 ± 0.2	5.1 ± 0.4	4.2 ± 0.2	40 ± 5	0.103

Specifically, O-VMA1.0, O-VMA1.5, and O-VMA2.0 are 40.7 %, 50.0 % and 27.2 % higher than those of R-VMA1.0, R-VMA1.5 and R-VMA2.0 respectively. This can be attributed to the reduced porosity as reported in Section 3.4.

Following the first crack, there is an upward and downward fluctuation of the stress along with the strain increasing. This leads to an increased strength, which is referred to as strain-hardening behavior [64]. The count of cracks is able to be computed according to the quantity of stress fluctuations [65]. The amplitude of stress fluctuations on the stress-strain curve is primarily effected by matrix strength and fiber-bridging capacity [66,67]. The presence of fine cracks is indicative of smaller stress fluctuations in the curve, as well as enhanced strain-hardening behavior. Compared with the conventional specimens, flow-induced specimens exhibit much smaller stress drop, see Fig. 17. 18, 25, 27, and 22 cracks are observed in R-VMA0.5, R-VMA1.0, R-VMA1.5 and R-VMA2.0, respectively, with the average crack widths of 0.178, 0.128, 0.148, and 0.136. The flow-induced specimens exhibit a larger count of cracks than the conventional specimens. The count of cracks observed in O-VMA0.5, O-VMA1.0, O-VMA1.5, and O-VMA2.0 is 29, 46, 37, and 40, respectively. The crack width is 0.124, 0.09, 0.097, and 0.103 mm, respectively, which is much smaller than that of the R series. This confirms that the enhanced fiber alignment achieved through the flow-induced casting approach increases the fiber-bridging capacity [18,68].

The stress-strain curve continues to evolve until achieving the peak stress, termed as ultimate tensile strength (UTS), and the corresponding strain is termed as tensile strain capacity (TSC). Table 7 shows the UTS and TSC of SHAAC. Compared to the conventional cast specimens with the same VMA dosage, the UTS of the O-VMA0.5, O-VMA1.0, O-VMA1.5, O-VMA2.0 specimens increased by 10.0 %, 35.6 %, 31.5 %, and 30.7 %, respectively, and the TSC increased by 18.4 %, 37.5 %, 14.3 %, and 13.5 %, respectively.

Notably, O-VMA1.0 exhibited the most pronounced enhancement. Its UTS and TSC can reach 6.1 MPa and 5.5 %, respectively. In the course of the uniaxial tensile test, after the initial cracking, the uniform dispersion of fibers within the matrix facilitates saturated multiple cracking. Moreover, a greater count of fibers aligned in the tensile direction allows more fibers to contribute to fiber bridging, and the reduction in matrix voids increased the bonding area between fibers and the matrix, improving the fiber/matrix interfacial properties, thereby enhancing the ultimate tensile properties [69,70]. This ultimately results in the optimal strain-hardening behavior observed in the O-VMA1.0 specimen.

Fig. 18 presents the strain field visualized by the DIC. All the proportions exhibit multiple cracking behavior. Clearly, the flow-induced cast specimens exhibit more saturated multiple cracking behavior and enhanced deformability compared to the conventional cast ones.

3.6. Empirical equation for tensile properties based on the features of fiber distribution

The strain-hardening and saturated multiple cracking behavior of SHAAC is governed by the combined effect of fiber distribution, orientation, and porosity. An empirical equation in the form of (Eq. 8) is proposed to predict tensile performance based on the aforementioned three parameters.

$$S = a\alpha\exp^{(b\eta)}(1 - cP) + d \tag{8}$$

where S is the ultimate tensile strength (MPa) / tensile strain capacity (%), α (unit-less) is the fiber distribution factor, η (unit-less) is the fiber orientation factor, P(%) is the measured porosity of SHAAC, a, b, c, d are the constants that can be fit using the experimental results.

Orthogonal distance regression was used to fit the equation. The fitting results are shown in Table 8, yielding determination coefficients (R^2) greater than 0.99. Fig. 19 compares the UTS and TSC values predicted by the proposed equation with the measured values. Overall, the predicted values demonstrate strong correlation with the measured values, with the deviation between prediction and experiment being less than 10 %.

The mathematical form of the equation is scientifically valid. However, since the empirical equation proposed in this study for predicting the tensile properties of SHAAC was derived based on the specific material composition and experimental conditions, re-fitting of its parameters is therefore required when applied to SHAAC with substantially different mix proportions.

4. Conclusions

In this study, the rheological properties of SHAAC were adjusted through the addition of different dosages of VMA. Impact of casting approach and rheological properties on the fiber distribution and alignment was investigated. Additionally, performance of SHAAC with different fiber spatial distributions under tension was evaluated.

(1) The distribution and orientation of PVA fibers in SHAAC are significantly influenced by the rheological properties of the paste. Fiber distribution and orientation factors reach the maximum at a VMA dosage of 1.0 % for both conventional and flow-induced casting approaches. In contrast to the conventional casting approach, the flow-induced approach further improves the fiber distribution and enhances the alignment of fibers in the flow direction. These two factors can be as high as 0.91 and 0.83, respectively.

(2) As YS and PV increase, a higher shear force is generated and acts as a guiding force. Along with another force generated by the screw pump, they drive fibers to rotate and disperse within the matrix. This facilitates fiber alignment during flow-induced casting, when the paste is extruded through the steel nozzle. The steel nozzle also restricts outward fiber movement, further enhancing fiber dispersion. However, once the YS reaches 192 Pa and the PV reaches 17.6 Pa·s, the shear force turns into a resistance. It prevents free fiber rotation, negatively affects the steel nozzle's wall effect, and ultimately reduces both the fiber distribution and orientation factors.
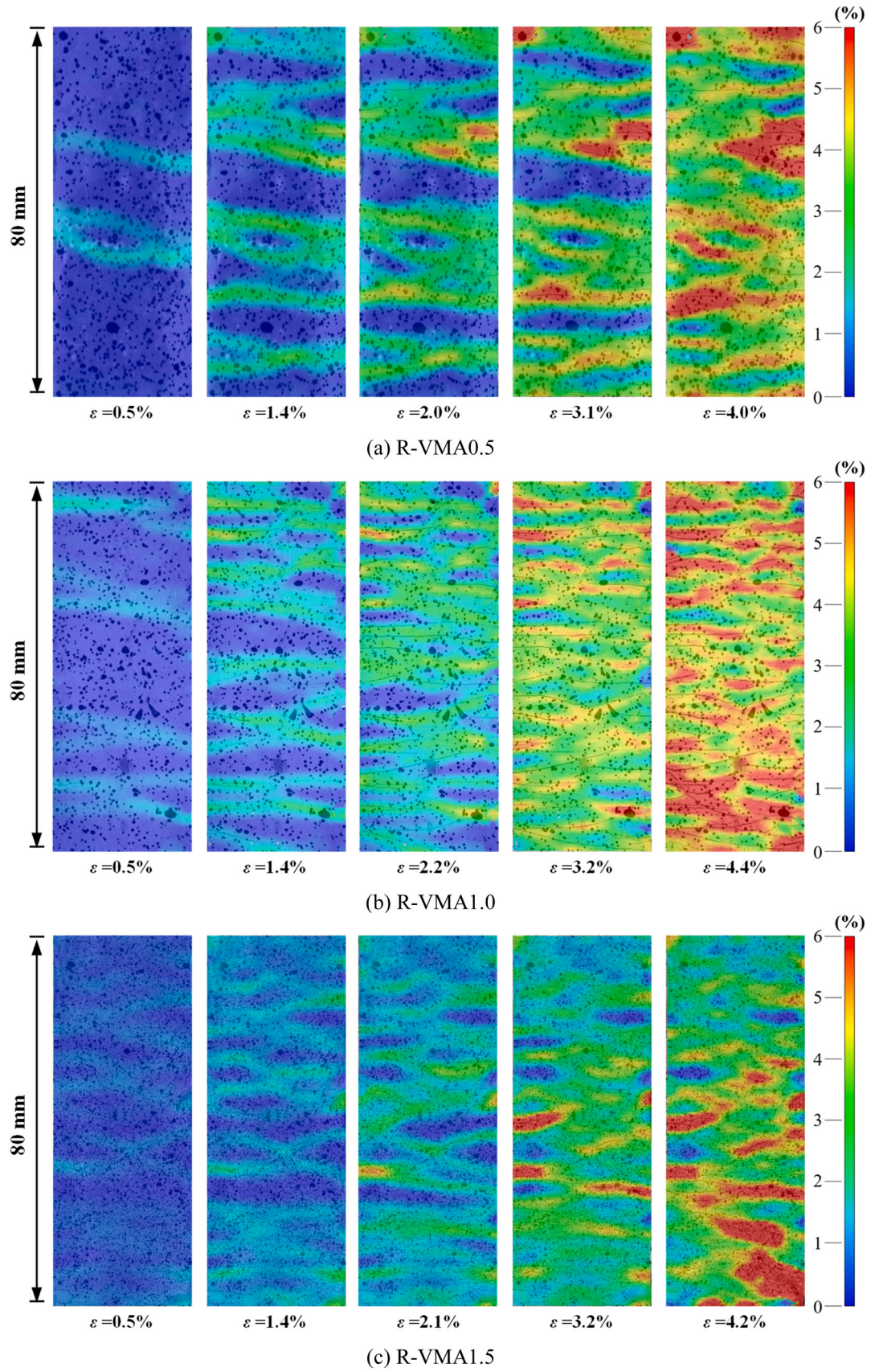
(a) R-VMA0.5

(b) R-VMA1.0

(c) R-VMA1.5

Fig. 18. DIC strain fields and crack patterns of SHAAC specimens at different tensile strain levels (The color bar represents the local tensile strain).
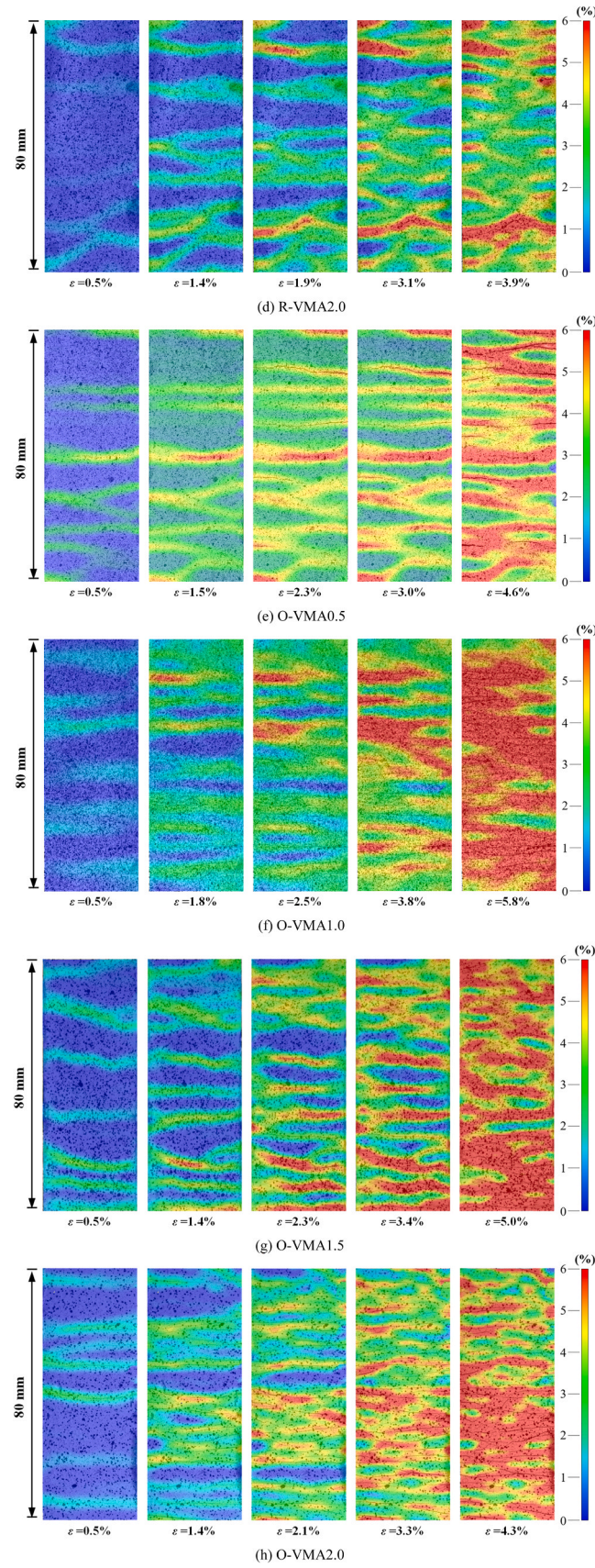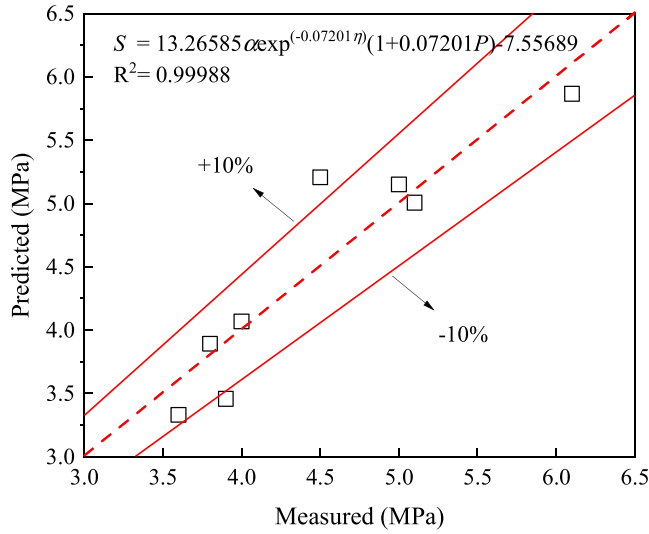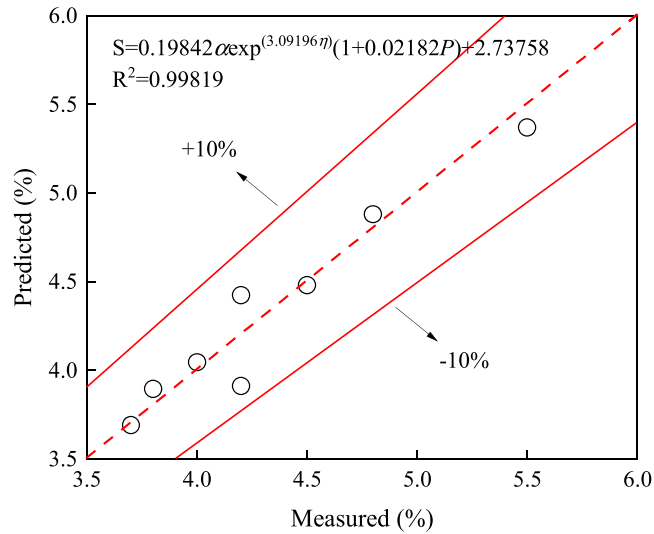
(d) R-VMA2.0

(e) O-VMA0.5

(f) O-VMA1.0

(g) O-VMA1.5

(h) O-VMA2.0

Fig. 18. (*continued*).

Table 8

Fitting results of tensile properties.

S	a	b	c	d	R^2
Ultimate tensile strength	13.26585	−0.00371	−0.07201	−7.55689	0.99988
Tensile strain capacity	0.19842	3.09196	−0.02182	2.73758	0.99819

$$S = 13.26585\alpha\exp^{(-0.07201\eta)}(1+0.07201P)-7.55689$$
$$R^2 = 0.99988$$

(a)

$$S = 0.19842\alpha\exp^{(3.09196\eta)}(1+0.02182P)+2.73758$$
$$R^2 = 0.99819$$

(b)

Fig. 19. Comparison of predicted and measured results of (a) ultimate tensile strength; and (b) tensile strain capacity.

(3) Using flow-induced casting approach, SHAAC (O-VMA1.0) with ultimate tensile stress and tensile strain capacity reached 6.1 MPa and 5.5 % can be prepared, showing enhancements of 36 % and 37 %, respectively, compared to the conventional casting approach (R-VMA1.0). This is accompanied with increased initial cracking strength and crack numbers, and reduced crack width.

(4) An equation was formulated to predict the ultimate tensile strength and tensile strain capacity, considering the fiber distribution factor, fiber orientation factor, and porosity. The determination coefficients (R^2) are greater than 0.99. The discrepancy between the predicted and measured values is restricted to under 10 %.

CRediT authorship contribution statement

Hongzhi Zhang: Writing – review & editing, Project administration, Methodology, Funding acquisition. **Branko Šavija:** Writing – review & editing, Supervision. **Zhi Ge:** Writing – original draft, Resources, Project administration, Methodology, Investigation, Formal analysis, Conceptualization. **Haomeng Song:** Writing – original draft, Visualization, Validation, Data curation, Conceptualization. **Jinlong Wang:** Visualization, Supervision, Resources, Investigation, Conceptualization. **Zhong Wang:** Visualization, Validation, Resources, Funding acquisition. **Hanming Zhang:** Writing – review & editing, Project administration, Methodology, Investigation.

Declaration of Competing Interest

The authors declare that they have no known competing financial interests or personal relationships that could have appeared to influence the work reported in this paper.

Data Availability

Data will be made available on request.

References

[1] V.C. Li, Engineered Cementitious Composites (ECC): Bendable Concrete for Sustainable and Resilient Infrastructure, Springer Berlin, 2019, https://doi.org/10.1007/978-3-662-58438-5.

[2] J.C. Lao, B.T. Huang, Y. Fang, L.Y. Xu, J.G. Dai, S.P. Shah, Strain-hardening alkali-activated fly ash/slag composites with ultra-high compressive strength and ultra-high tensile ductility, Cem. Concr. Res. 165 (2023) 18, https://doi.org/10.1016/j.cemconres.2022.107075.

[3] J.L. Provis, S.A. Bernal, Geopolymers and related alkali-activated materials, Annu. Rev. Mater. Res. 44 (1) (2014) 299–327, https://doi.org/10.1146/annurev-matsci-070813-113515.

[4] S. Zhang, V.C. Li, G. Ye, Micromechanics-guided development of a slag/fly ash-based strain-hardening geopolymer composite, Cem. Concr. Compos. 109 (2020), https://doi.org/10.1016/j.cemconcomp.2020.103510.

[5] P. Duxson, J.L. Provis, G.C. Lukey, S.W. Mallicoat, W.M. Kriven, J.S.J. van Deventer, Understanding the relationship between geopolymer composition, microstructure and mechanical properties, Colloids Surf. A Physicochem. Eng. Asp. 269 (1-3) (2005) 47–58, https://doi.org/10.1016/j.colsurfa.2005.06.060.

[6] J. Zhao, L. Tong, B. Li, T. Chen, C. Wang, G. Yang, Y. Zheng, Eco-friendly geopolymer materials: a review of performance improvement, potential application and sustainability assessment, J. Clean. Prod. 307 (2021), https://doi.org/10.1016/j.jclepro.2021.127085.

[7] M. Nedeljković, M. Luković, K. van Breugel, D. Hordijk, G. Ye, Development and application of an environmentally friendly ductile alkali-activated composite, J. Clean. Prod. 180 (2018) 524–538, https://doi.org/10.1016/j.jclepro.2018.01.162.

[8] Y. Wang, H. Zhong, M. Zhang, Experimental study on static and dynamic properties of fly ash-slag based strain hardening geopolymer composites, Cem. Concr. Compos. 129 (2022), https://doi.org/10.1016/j.cemconcomp.2022.104481.

[9] P. Sturm, S. Greiser, G.J.G. Gluth, C. Jäger, H.J.H. Brouwers, Degree of reaction and phase content of silica-based one-part geopolymers investigated using chemical and NMR spectroscopic methods, J. Mater. Sci. 50 (20) (2015) 6768–6778, https://doi.org/10.1007/s10853-015-9232-5.

[10] C. Shi, D. Roy, Alkali-activated cements and concretes, Taylor Fr., Abingdon UK (2006), https://doi.org/10.1201/9781482266900.

[11] S.-J. Choi, J.-I. Choi, J.-K. Song, B.Y. Lee, Rheological and mechanical properties of fiber-reinforced alkali-activated composite, Constr. Build. Mater. 96 (2015) 112–118, https://doi.org/10.1016/j.conbuildmat.2015.07.182.

[12] M. Ohno, V.C. Li, An integrated design method of engineered geopolymer composite, Cem. Concr. Compos. 88 (2018) 73–85, https://doi.org/10.1016/j.cemconcomp.2018.02.001.

[13] S.F.A. Shah, B. Chen, S.Y. Oderji, M. Aminul Haque, M.R. Ahmad, Comparative study on the effect of fiber type and content on the performance of one-part alkali-activated mortar, Constr. Build. Mater. 243 (2020), https://doi.org/10.1016/j.conbuildmat.2020.118221.

[14] Q. Wang, Y. Yi, G. Ma, H. Luo, Hybrid effects of steel fibers, basalt fibers and calcium sulfate on mechanical performance of PVA-ECC containing high-volume fly ash, Cem. Concr. Compos. 97 (2019) 357–368, https://doi.org/10.1016/j.cemconcomp.2019.01.009.

[15] K. Bilisik, H. Ozdemir, Multiaxis three dimensional (3D) carbon and basalt preforms/cementitious matrix concretes: experimental study on fiber orientation and placement by panel test, Constr. Build. Mater. 271 (2021), https://doi.org/10.1016/j.conbuildmat.2020.121863.

[16] H.T. Thanh, J. Li, Y.X. Zhang, Numerical modelling of the flow of self-consolidating engineered cementitious composites using smoothed particle hydrodynamics, Constr. Build. Mater. 211 (2019) 109–119, https://doi.org/10.1016/j.conbuildmat.2019.03.210.

[17] J.-I. Choi, B. Lee, Bonding properties of basalt fiber and strength reduction according to fiber orientation, Materials 8 (10) (2015) 6719–6727, https://doi.org/10.3390/ma8105335.

[18] C. Ding, L. Guo, B. Chen, Orientation distribution of polyvinyl alcohol fibers and its influence on bridging capacity and mechanical performances for high ductility cementitious composites, Constr. Build. Mater. 247 (2020), https://doi.org/10.1016/j.conbuildmat.2020.118491.

[19] V.P. Villar, N.F. Medina, M.M. Alonso, S.G. Diez, F. Puertas, Assessment of parameters governing the steel fiber alignment in fresh cement-based composites, Constr. Build. Mater. 207 (2019) 548–562, https://doi.org/10.1016/j.conbuildmat.2019.02.036.

[20] F. Laranjeira, A. Aguado, C. Molins, S. Grünewald, J. Walraven, S. Cavalaro, Framework to predict the orientation of fibers in FRC: a novel philosophy, Cem. Concr. Res. 42 (6) (2012) 752–768, https://doi.org/10.1016/j.cemconres.2012.02.013.

[21] P.F.G. Banfill, Rheological methods for assessing the flow properties of mortar and related materials, Constr. Build. Mater. 8 (1) (1994) 43–50, https://doi.org/10.1016/0950-0618(94)90007-8.

[22] M. Li, V.C. Li, Rheology, fiber dispersion, and robust properties of engineered cementitious composites, Mater. Struct. 46 (3) (2012) 405–420, https://doi.org/10.1617/s11527-012-9909-z.

[23] K. Tosun-Felekoğlu, B. Felekoğlu, R. Ranade, B.Y. Lee, V.C. Li, The role of flaw size and fiber distribution on tensile ductility of PVA-ECC, Compos. Part B: Eng. 56 (2014) 536–545, https://doi.org/10.1016/j.compositesb.2013.08.089.

[24] E.-H. Yang, M. Sahmaran, Y. Yang, V. C.Li, Rheological Control in Production of Engineered Cementitious Composites, Acids Mater. J. 106 (4) (2009) 357–366, https://doi.org/10.14359/56656.

[25] M. Şahmaran, Z. Bilici, E. Ozbay, T.K. Erdem, H.E. Yucel, M. Lachemi, Improving the workability and rheological properties of Engineered Cementitious Composites using factorial experimental design, Compos. Part B: Eng. 45 (1) (2013) 356–368, https://doi.org/10.1016/j.compositesb.2012.08.015.

[26] R. Flatt, I. Schober, Superplasticizers and the rheology of concrete, Woodhead Publ. Ltd, Camb. (2012), https://doi.org/10.1533/9780857095282.2.144.

[27] Z. Tang, C. Litina, A. Al-Tabbaa, Optimisation of rheological parameters and mechanical properties of Engineered Cementitious Composites (ECC) using regression-based models, Constr. Build. Mater. 310 (2021), https://doi.org/10.1016/j.conbuildmat.2021.125281.

[28] L.F. Maya Duque, B. Graybeal, Fiber orientation distribution and tensile mechanical response in UHPFRC, Mater. Struct. 50 (1) (2016), https://doi.org/10.1617/s11527-016-0914-5.

[29] G. Ma, Z. Li, L. Wang, F. Wang, J. Sanjayan, Mechanical anisotropy of aligned fiber reinforced composite for extrusion-based 3D printing, Constr. Build. Mater. 202 (2019) 770–783, https://doi.org/10.1016/j.conbuildmat.2019.01.008.

[30] H.M.E. Afefy, M.H. Mahmoud, Structural performance of RC slabs provided by pre-cast ECC strips in tension cover zone, Constr. Build. Mater. 65 (2014) 103–113, https://doi.org/10.1016/j.conbuildmat.2014.04.096.

[31] D.G. Soltan, V.C. Li, A self-reinforced cementitious composite for building-scale 3D printing, Cem. Concr. Compos. 90 (2018) 1–13, https://doi.org/10.1016/j.cemconcomp.2018.03.017.

[32] H. Ma, Z.G. Zhang, Paving an engineered cementitious composite (ECC) overlay on concrete airfield pavement for reflective cracking resistance, Constr. Build. Mater. 252 (2020) 10, https://doi.org/10.1016/j.conbuildmat.2020.119048.

[33] M. Rutzen, P. Lauff, R. Niedermeier, O. Fischer, M. Raith, C.U. Grosse, U. Weiss, M. A. Peter, D. Volkmer, Influence of fiber alignment on pseudoductility and microcracking in a cementitious carbon fiber composite material, Mater. Struct. 54 (2) (2021), https://doi.org/10.1617/s11527-021-01649-2.

[34] J.J. Martin, M.S. Riederer, M.D. Krebs, R.M. Erb, Understanding and overcoming shear alignment of fibers during extrusion, Soft Matter 11 (2) (2015) 400–405, https://doi.org/10.1039/c4sm02108h.

[35] Z.M. Pang, C. Lu, B.S. Li, J.J. Wang, A multiscale model for quantifying fiber orientation effects on the tensile properties of 3D printed Engineered Cementitious Composites (3DP-ECC), J. Build. Eng. 68 (2023) 15, https://doi.org/10.1016/j.jobe.2023.106090.

[36] C. Lu, C.K.Y. Leung, Theoretical evaluation of fiber orientation and its effects on mechanical properties in Engineered Cementitious Composites (ECC) with various thicknesses, Cem. Concr. Res. 95 (2017) 240–246, https://doi.org/10.1016/j.cemconres.2017.02.024.

[37] B. Boulekbache, M. Hamrat, M. Chemrouk, S. Amziane, Flowability of fibre-reinforced concrete and its effect on the mechanical properties of the material, Constr. Build. Mater. 24 (9) (2010) 1664–1671, https://doi.org/10.1016/j.conbuildmat.2010.02.025.

[38] V.C. Li, F.P. Bos, K. Yu, W. McGee, T.Y. Ng, S.C. Figueiredo, K. Nefs, V. Mechtcherine, V.N. Nerella, J. Pan, G.P.A.G. van Zijl, P.J. Kruger, On the emergence of 3D printable Engineered, Strain Hardening Cementitious Composites (ECC/SHCC), Cem. Concr. Res. 132 (2020), https://doi.org/10.1016/j.cemconres.2020.106038.

[39] S. Parviz, L. Cha-Don, Distribution and Orientation of Fibers in Steel Fiber Reinforced Concrete, Acids Mater. J. 87 (5) (1990), https://doi.org/10.14359/1803.

[40] D. Dupont, L. Vandewalle, Distribution of steel fibres in rectangular sections, Cem. Concr. Compos. 27 (3) (2005) 391–398, https://doi.org/10.1016/j.cemconcomp.2004.03.005.

[41] A.M. Tawfek, Z. Ge, H. Yuan, N. Zhang, H. Zhang, Y. Ling, Y. Guan, B. Šavija, Influence of fiber orientation on the mechanical responses of engineering cementitious composite (ECC) under various loading conditions, J. Build. Eng. 63 (2023), https://doi.org/10.1016/j.jobe.2022.105518.

[42] K.J. Trainor, B.W. Foust, E.N. Landis, Measurement of Energy Dissipation Mechanisms in Fracture of Fiber-Reinforced Ultrahigh-Strength Cement-Based Composites, J. Eng. Mech. 139 (7) (2013) 771–779, https://doi.org/10.1061/(asce)em.1943-7889.0000545.

[43] A. Nagura, K. Okamoto, K. Itoh, Y. Imai, D. Shimamoto, Y. Hotta, The Ni-plated carbon fiber as a tracer for observation of the fiber orientation in the carbon fiber reinforced plastic with X-ray CT, Compos. Pt. B-Eng. 76 (2015) 38–43, https://doi.org/10.1016/j.compositesb.2015.02.009.

[44] T. Oesch, E. Landis, D. Kuchma, A methodology for quantifying the impact of casting procedure on anisotropy in fiber-reinforced concrete using X-ray CT, Mater. Struct. 52 (2) (2019) 1, https://doi.org/10.1617/s11527-019-1339-8.

[45] H.T. Thanh, Modelling Flowable Engineered Cementitious Composites and its Fibre Orientation and Distribution for Tensile, Perform. Eval. (2021) https://doi.org/hdl.handle.net/10453/151031.

[46] J. Han, Z. Miao, J. Wang, X. Zhang, Y. Lv, Investigation of the corrosion-induced damage mechanism of steel fibers in ultra-high-performance steel fiber-reinforced concrete using X-ray computed tomography, Constr. Build. Mater. 368 (2023), https://doi.org/10.1016/j.conbuildmat.2023.130429.

[47] E.S.L. Gastal, M.M. Oliveira, Adaptive manifolds for real-time high-dimensional filtering, ACM Trans. Graph. 31 (4) (2012) 1–13, https://doi.org/10.1145/2185520.2185529.

[48] B. Šavija, M. Luković, S.A.S. Hosseini, J. Pacheco, E. Schlangen, Corrosion induced cover cracking studied by X-ray computed tomography, nanoindentation, and energy dispersive X-ray spectrometry (EDS), Mater. Struct. 48 (7) (2014) 2043–2062, https://doi.org/10.1617/s11527-014-0292-9.

[49] H. Zhao, T. Zhao, Z. Ning, R. Zhang, T. Duan, Q. Wang, P. Lian, D. Zhang, W. Zhang, Petrophysical characterization of tight oil sandstones by microscale X-ray computed tomography, Mar. Pet. Geol. 102 (2019) 604–614, https://doi.org/10.1016/j.marpetgeo.2019.01.029.

[50] D.M. Stasiw, F.B. Cook, M.C. Detraglia, L.C. Cerny, DRAG AND SPHERICITY INDEX OF A SPINDLE, Q. Appl. Math. 32 (3) (1974) 351–354, https://doi.org/10.1090/qam/99675.

[51] J. Kastner, B. Harrer, H.P. Degischer, High resolution cone beam X-ray computed tomography of 3D-microstructures of cast Al-alloys, Mater. Charact. 62 (1) (2011) 99–107, https://doi.org/10.1016/j.matchar.2010.11.004.

[52] X. Zhou, N. Dai, X. Cheng, A. Thompson, R. Leach, Three-dimensional characterization of powder particles using X-ray computed tomography, Addit. Manuf. 40 (2021), https://doi.org/10.1016/j.addma.2021.101913.

[53] F. Forster, R. Hegerl, Structure determination in situ by averaging of tomograms, Methods Cell Biol. 79 (2007) 741–767, https://doi.org/10.1016/s0091-679x(06)79029-x.

[54] A. Rigort, D. Guenther, R. Hegerl, D. Baum, B. Weber, S. Prohaska, O. Medalia, W. Baumeister, H.-C. Hege, Automated segmentation of electron tomograms for a quantitative description of actin filament networks, J. Struct. Biol. 177 (1) (2012) 135–144, https://doi.org/10.1016/j.jsb.2011.08.012.

[55] K. Schönlin, Ermittlung der Orientierung, Menge und Verteilung der Fasern in faserbewehrtem Beton, Beton- und Stahlbetonbau 83 (6) (1988) 168–171, https://doi.org/10.1002/best.198800280.

[56] M. Xia, H. Hamada, Z. Maekawa, Flexural Stiffness of Injection Molded Glass Fiber Reinforced Thermoplastics, Int. Polym. Process. 10 (1) (1995) 74–81, https://doi.org/10.3139/217.950074.

[57] J. Zhou, S. Qian, G. Ye, O. Copuroglu, K. van Breugel, V.C. Li, Improved fiber distribution and mechanical properties of engineered cementitious composites by adjusting the mixing sequence, Cem. Concr. Compos. 34 (3) (2012) 342–348, https://doi.org/10.1016/j.cemconcomp.2011.11.019.

[58] M. Li, P. Yan, J. Han, L. Guo, Which Is an Appropriate Quadratic Rheological Model of Fresh Paste, the Modified Bingham Model or the Parabolic Model? Processes 10 (12) (2022) https://doi.org/10.3390/pr10122603.

[59] H. Bessaies-Bey, K.H. Khayat, M. Palacios, W. Schmidt, N. Roussel, Viscosity modifying agents: Key components of advanced cement-based materials with adapted rheology, Cem. Concr. Res. 152 (2022), https://doi.org/10.1016/j.cemconres.2021.106646.

[60] Y. Bai, Y. Bai, J. Tang, H. Su, F. Zhang, H. Ma, L. Ge, Y. Cai, Effects of hydroxypropyl methylcellulose on anti-dispersion and rheology of alkali-activated materials in underwater engineering, Constr. Build. Mater. 393 (2023), https://doi.org/10.1016/j.conbuildmat.2023.132135.

[61] H.H. Nguyễn, J.-I. Choi, H.-K. Kim, B.Y. Lee, Mechanical properties and self-healing capacity of eco-friendly ultra-high ductile fiber-reinforced slag-based composites, Compos. Struct. 229 (2019), https://doi.org/10.1016/j.compstruct.2019.111401.

[62] B. Łaźniewska-Piekarczyk, Effect of viscosity type modifying admixture on porosity, compressive strength and water penetration of high performance self-compacting concrete, Constr. Build. Mater. 48 (2013) 1035–1044, https://doi.org/10.1016/j.conbuildmat.2013.07.076.

[63] S.C. Figueiredo, O. Çopuroglu, E. Schlangen, Effect of viscosity modifier admixture on Portland cement paste hydration and microstructure, Constr. Build. Mater. 212 (2019) 818–840, https://doi.org/10.1016/j.conbuildmat.2019.04.020.

[64] Y. Wang, F. Liu, J. Yu, F. Dong, J. Ye, Effect of polyethylene fiber content on physical and mechanical properties of engineered cementitious composites, Constr. Build. Mater. 251 (2020), https://doi.org/10.1016/j.conbuildmat.2020.118917.

[65] B. Shan, S. Zheng, J. Ou, A stereovision-based crack width detection approach for concrete surface assessment, KSCE J. Civ. Eng. 20 (2) (2015) 803–812, https://doi.org/10.1007/s12205-015-0461-6.

[66] L. Teng, H. Huang, J. Du, K.H. Khayat, Prediction of fiber orientation and flexural performance of UHPC based on suspending mortar rheology and casting method, Cem. Concr. Compos. 122 (2021), https://doi.org/10.1016/j.cemconcomp.2021.104142.

[67] B.-T. Huang, K.-F. Weng, J.-X. Zhu, Y. Xiang, J.-G. Dai, V.C. Li, Engineered/strain-hardening cementitious composites (ECC/SHCC) with an ultra-high compressive strength over 210 MPa, Compos. Commun. 26 (2021), https://doi.org/10.1016/j.coco.2021.100775.

[68] V.C. Li, C.K.Y. Leung, STEADY-STATE AND MULTIPLE CRACKING OF SHORT RANDOM FIBER COMPOSITES, J. Eng. Mech. -ASCE 118 (11) (1992) 2246–2264, https://doi.org/10.1061/(asce)0733-9399(1992)118:11(2246).

[69] B. Felekoğlu, K. Tosun-Felekoğlu, E. Gödek, A novel method for the determination of polymeric micro-fiber distribution of cementitious composites exhibiting multiple cracking behavior under tensile loading, Constr. Build. Mater. 86 (2015) 85–94, https://doi.org/10.1016/j.conbuildmat.2015.03.094.

[70] Q. Fan, Y. Zheng, C. He, D. Meng, Q. Guo, Y. Liu, Effect of interfacial properties between polyethylene and polyvinyl alcohol fiber/cement matrix on properties of mortar and ECC, Struct. Concr. (2024), https://doi.org/10.1002/suco.202400607.